Patient-Specific Modeling and Quantification of the Aortic and Mitral Valves from 4D Cardiac CT and TEE

Razvan Ioan Ionasec[1,2], Ingmar Voigt[1,3], Bogdan Georgescu[1]
Yang Wang[1], Helene Houle[4], Fernando Vega-Higuera[5], Nassir Navab[2], and Dorin Comaniciu[1]

[1]Integrated Data Systems Department, Siemens Corporate Research, Princeton NJ, USA
[2]Computer Aided Medical Procedures, Technical University Munich, Germany
[3]Chair of Pattern Recognition, University of Erlangen-Nuremberg, Germany
[4]Siemens Healthcare Ultrasound, Mountain View CA, USA
[5]Siemens Healthcare Computed Tomography, Forchheim, Germany

Corresponding Author: Razvan Ioan Ionasec
E-mail: razvan.ionasec@siemens.com
Phone: 1-609-734-3750, Fax: 1-609-734-6565

Abstract— As decisions in cardiology increasingly rely on non-invasive methods, fast and precise image processing tools have become a crucial component of the analysis workflow. *To the best of our knowledge,* we propose the first automatic system for patient-specific modeling and quantification of the left heart valves, which operates on cardiac computed tomography (CT) and transesophageal echocardiogram (TEE) data. Robust algorithms, based on recent advances in discriminative learning, are used to estimate patient-specific parameters from sequences of volumes covering an entire cardiac cycle. A novel physiological model of the aortic and mitral valves is introduced, which captures complex morphologic, dynamic and pathologic variations. This holistic representation is hierarchically defined on three abstraction levels: global location and rigid motion model, non-rigid landmark motion model and comprehensive aortic-mitral model. First we compute the rough location and cardiac motion applying marginal space learning. The rapid and complex motion of the valves, represented by anatomical landmarks, is estimated using a novel trajectory spectrum learning algorithm. The obtained landmark model guides the fitting of the full physiological valve model, which is locally refined through learned boundary detectors. Measurements efficiently computed from the aortic-mitral representation support an effective morphological and functional clinical evaluation. Extensive experiments on a heterogeneous data set, cumulated to 1516 TEE volumes from 65 4D TEE sequences and 690 cardiac CT volumes from 69 4D CT sequences, demonstrated a speed of 4.8 seconds per volume and average accuracy of 1.45mm with respect to expert defined ground-truth. Additional clinical validations prove the quantification precision to be in the range of inter-user variability. To the best of our knowledge this is the first time a patient-specific model of the aortic and mitral valves is automatically estimated from volumetric sequences.

Index Terms— Heart Valve Modeling, Heart Valve Quantification, Trajectory Spectrum Learning, Non-Rigid Motion Estimation, Patient-Specific Modeling

I. INTRODUCTION

Valvular surgery accounts for up to 20% of all cardiac procedures in the United States and is applied in nearly 100,000 patients every year. Yet, with an average cost of $120,000 and 5.6% in hospital death rate, valve operations are the most expensive and riskiest cardiac interventions [1]. Aortic and mitral valves are most commonly affected, cumulating in 64% and 15%, respectively of all valvular heart disease (VHD) cases [2].

The heart valves play a key role in the cardiovascular system as they regulate the blood flow inside the heart chambers and human body. In particular, the aortic and mitral valves execute synchronized rapid opening and closing movements to govern the fluid interaction in-between the left atrium (LA), left ventricle (LV) and aorta (Ao). Their complex morphological, functional and hemodynamical interdependency has been recently underlined [3], [4].

Congenital, degenerative, structural, infective or inflammatory diseases can provoke dysfunctions, resulting in stenotic and regurgitant valves [5]. The blood flow is obstructed or, in case of regurgitant valves, blood leaks due to improper closing. Both conditions can greatly interfere with the pumping function of the heart, causing life-threatening conditions. Severe cases require valve surgery, while mild to moderate cases need accurate diagnosis and long-term medical management.

Precise morphological and functional knowledge about the aortic-mitral apparatus is a prerequisite during the entire clinical workflow including diagnosis, therapy-planning, surgery or percutaneous intervention as well as patient monitoring and follow-up. To date, most non-invasive investigations are based on two-dimensional images, user-dependent processing and manually performed, potentially inaccurate measurements [2]. Imaging modalities, such as Cardiac Computed Tomography (CT) and Transesophageal Echocardiography (TEE), enable for dynamic four dimensional scans of the beating heart over the whole cardiac cycle. Such volumetric time-resolved data encodes comprehensive structural and dynamic information, which however is barely exploited in clinical practice, due
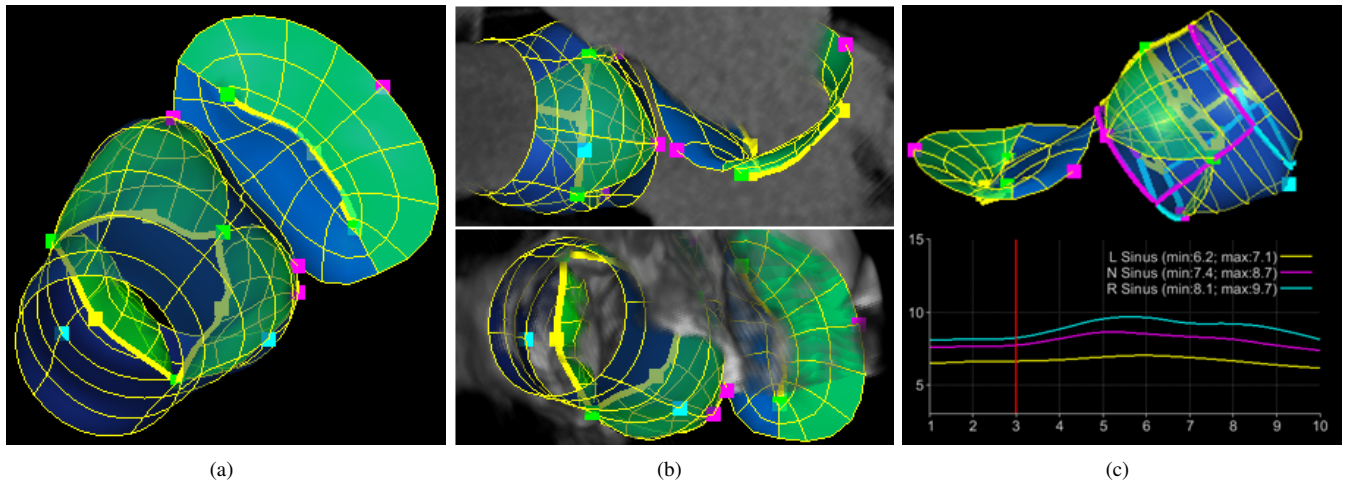
Fig. 1. (a) Physiological model of the aortic-mitral coupling, (b) Patient-specific model fitted to CT (top) and TEE (bottom) data, (c) example of model-driven quantification - volumes of the aortic valve sinuses over the cardiac cycle.

to its size and complexity as well as the lack of appropriate medical systems.

In this paper, we propose a novel system for patient-specific modeling and clinical assessment of the aortic and mitral valves. The robust conversion of four dimensional CT or TEE data into relevant morphological and functional quantities comprises three aspects: physiological modeling, patient-specific model estimation and model-driven quantification (see Fig. 1). The aortic-mitral coupling is represented through a mathematical model sufficiently descriptive and flexible to capture complex morphological, dynamic and pathological variation. It includes all major anatomic landmarks and structures and likewise it is hierarchically designed to facilitate automatic estimation of its parameters. Robust machine-learning algorithms process the four-dimensional data coming from the medical scanners and estimate patient-specific models of the valves. As a result, a wide-ranging automatic analysis can be performed to measure relevant morphological and functional aspects of the subject valves. In that context, our major contributions include:

- A **comprehensive physiologically-driven model** of the aortic and mitral valves to capture the full morphology and dynamics as well as pathologic variations.
- A robust and efficient method to **automatically estimate valve model parameters** from four-dimensional CT or TEE data. It includes a novel trajectory spectrum learning algorithm for localization and motion estimation of non-rigid objects.
- A model-driven and automatic analysis method, that supports for **morphological quantification and measurement of dynamic variations** over the entire cardiac cycle.
- **Simultaneous analysis of the aortic-mitral complex** for concomitant clinical management and in-depth understanding of the reciprocal functional influences.

Part of this work has been reported in our conference publications [6]–[8]. *In this paper, the joint valve model includes a physiologically-driven parameterization to represent the full morphology and dynamics of the aortic-mitral apparatus. It also introduces a complete framework for patient-specific parameter estimation from CT and TEE data. Moreover, a model-based valve quantification methodology is presented along with extensive clinical experiments.* The remainder of this paper is organized as follows: Sec. II offers an overview of previous work on modeling and detection of cardiac structures. The new physiological model of the aortic and mitral valves is presented in Sec III. In Sec. IV we introduce a robust algorithm for patient-specific modeling, which includes trajectory spectrum learning and local-spatio-temporal features. Model-driven valve quantification is presented in Sec. V. Experiments and clinical applications are discussed in Sec. VI. This paper concludes with Sec. VII.

II. RELATED WORK

This section presents the related work on heart valves and cardiac models as well as object detection and motion estimation applied to organs.

A. Cardiac and Valve Modeling

The majority of cardiac models to date are focusing on the representation of the left (LV) and the right ventricle (RV). More comprehensive models include also the left (LA) and right atrium (RA) [9], ventricular outflow tracts (LVOT and RVOT) [10], or the aorta (Ao) and pulmonary trunk (PA) [11]. Nevertheless, none of the mentioned references provides an explicit model of the aortic or mitral valve. Existent valve models presented in the literature are mostly generic and used for hemodynamic studies or analysis of various prostheses [12]–[16]. In [17], a model of the mitral valve used for manual segmentation of TEE data is presented. As it includes only the mitral valve annulus and closure line during systole, it is both static and simple. A representation of the aortic-mitral coupling was recently proposed in [18]. This model is dynamic but limited to only a curvilinear representation of the aortic and mitral annuli. Due to the narrow level of detail and insufficient parameterization, none of the existing valve models

are applicable for comprehensive patient-specific modeling or clinical assessment.

B. Estimation of Patient-Specific Dynamic Models

The model estimation determines patient-specific parameters from unseen volumetric sequences. Considering the anatomical and functional complexity of the heart valves, the estimation procedure can be divided into two tasks: object delineation and motion estimation.

Related approaches based on active shape models (ASM) [19], active appearance models (AAM) [20] or deformable models [21], [22] are generally applied for object delineation and segmentation *[23], [24]*. Often these methods involve semi-automatic inference or require manual initialization for object location. Recently, discriminative learning methods have been proved to efficiently solve localization problems by classifying image regions as containing a target object. In [10], the learning based approach is applied to three-dimensional object localization by introducing an efficient search method referred to as marginal space learning (MSL). To handle the large number of possible pose parameters of a 3D object, an exhaustive search of hypotheses is performed in sub-spaces with gradually increased dimensionality.

Instead of extending discriminative learning algorithms for time dependent four-dimensional problems, to date, motion estimation is approached by tracking methods. To improve robustness, many tracking algorithms integrate key frame detection [25]. The loose coupling between detector and tracker often outputs temporally inconsistent results. For a more effective search, strong dynamic [26] models or sophisticated statistical methods are incorporated in motion estimation algorithms [27].

Trajectory-based features have also increasingly attracted attention in motion analysis and recognition [28]. It has been shown that the inherent representative power of both shape and trajectory projections of non-rigid motion are equal, but the representation in the trajectory space can significantly reduce the number of parameters to be optimized [29]. This duality has been exploited in motion reconstruction and segmentation [30], structure from motion [29]. In particular, for periodic motion, frequency domain analysis shows promising results in motion estimation and recognition [31], [32]. Although the compact parameterization and duality property are crucial in the context of learning-based object detection and motion estimation, this synergy has not been fully exploited yet.

III. AORTIC-MITRAL PHYSIOLOGICAL MODELING

In this section we introduce our physiological model of the aortic and mitral valves, designed to capture complex morphological, dynamical and pathological variations. Its hierarchical definition is constructed on three abstraction levels: global location and rigid motion model, non-rigid landmark motion model, and comprehensive aortic-mitral model. Along with the parameterization, we introduce an anatomically driven resampling method, to establish point correspondence required for the construction of a statistical shape model.
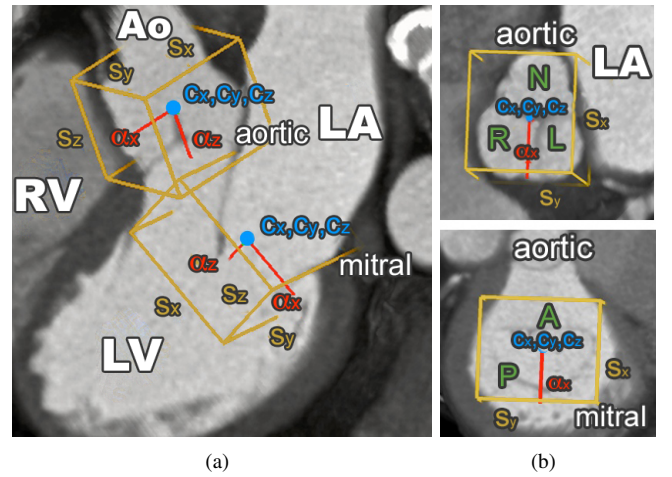

(a) (b)

Fig. 2. Bounding boxes for aortic and mitral valves encoding their individual translation (c_x, c_y, c_z), rotation $(\vec{\alpha_x}, \vec{\alpha_y}, \vec{\alpha_z})$ and scale (s_x, s_y, s_z). (a) Apical three chamber view, (b) aortic and mitral valves seen from the aorta and left atrium respectively, toward the LV. The green letters L,R,N and A,P indicate the L/R/N - aortic leaflets and anterior/posterior mitral leaflets, respectively.

A. Global Location and Rigid Motion Model

The global location of both aortic and mitral valves is parameterized through the similarity transformation in the three-dimensional space, illustrated as a bounding box in Fig. 2. A time variable t is augmenting the representation to capture the temporal variation during the cardiac cycle.

$$\theta = \{(c_x, c_y, c_z), (\vec{\alpha_x}, \vec{\alpha_y}, \vec{\alpha_z}), (s_x, s_y, s_z), t\} \quad (1)$$

where (c_x, c_y, c_z), $(\vec{\alpha_x}, \vec{\alpha_y}, \vec{\alpha_z})$, (s_x, s_y, s_z) are the position, orientation and scale parameters (Fig. 2). The remainder of the section describes the anatomically-driven definition of each parameter in θ for both valves. ***Please note that the rigid motion is modeled independently for the aortic and mitral valves.***

The **aortic valve** connects the left ventricular outflow tract to the ascending aorta and includes the aortic root and three leaflets/cusps (left (L) aortic leaflet, right (R) aortic leaflet and none (N) aortic leaflet). The root extends from the basal ring to the sinotubular junction and builds the supporting structure for the leaflets. These are fixed to the root on a crown-like attachment and can be thought of as semi-lunar pockets. The position parameter $(c_x, c_y, c_z)_{aortic}$ is given by the valve's barycenter, while the corresponding scale $(s_x, s_y, s_z)_{aortic}$ is chosen to comprise the entire underlying anatomy. The long axis $\vec{\alpha_z}$ is defined by the normal vectors to the aortic commissural plane, which is the main axis of the aortic root. The short axis $\vec{\alpha_x}$ is given by the normalized vector pointing from the barycenter $(c_x, c_y, c_z)_{aortic}$ to the interconnection point of the left and right leaflet, the left/right-commissure point. The $\vec{\alpha_y}$ direction is constructed from the cross-product of $\vec{\alpha_x}$ and $\vec{\alpha_z}$.

Located in between the left atrium and the left ventricle, the **mitral valve** includes the posterior leaflet, anterior leaflet, annulus and subvalvular apparatus. The latter consists of the chordae tendiae and papillary muscles, which are not explicitly treated in this work. Hence, we compute the barycentric posi-

tion $(c_x, c_y, c_z)_{mitral}$ and scale parameters $(s_x, s_y, s_z)_{mitral}$ from the mitral leaflets. $\vec{\alpha}_z$ is described by the normal vector to the mitral annulus, while $\vec{\alpha}_x$ points from the barycenter $(c_x, c_y, c_z)_{mitral}$ toward the postero-annular midpoint.

In practice, the ground truth of the global location and rigid motion model is described by the anatomical landmarks. Landmarks and their relation to the global location and rigid motion are defined in the next section III-B.

B. Non-rigid Landmark Motion Model

The aortic and mitral valves execute a rapid opening-closing movement, which follows a complex and synchronized motion pattern. Normalized by the time-dependent similarity transformation introduced in Sec. III-A, the non-rigid motion is represented through a model consisting of 18 anatomically-defined landmarks (see Fig. 3). Three aortic commissure points, LR-Comm, NL-Comm and RN-Comm, describe the interconnection locations of the aortic leaflets, while three hinges, L-Hinge, R-Hinge, and N-Hinge, are their lowest attachment points to the root. For each leaflet of the aortic and mitral valves, the center of the corresponding free-edge is marked by the leaflet tip point: L/R/N-Tip tips for aortic valves and Ant/Post-Tip (anterior/posterior) leaflet tips for mitral valves. The two interconnection points of the mitral leaflets at their free edges are defined by the mitral Ant/Post-Comm, while the mitral annulus is fixed by the L/R-Trigone and posteroannular midpoint (PostAnn MidPoint). Finally, the interface between the aorta and coronary arteries is symbolized using the L/R-Ostium, the two coronary ostia. ***Besides the well defined anatomical meaning, the chosen landmarks serve as anchor points for qualitative and quantitative clinical assessment, are robustly identifiable by doctors and possess a particular visual pattern.***

Given the previous description, the motion of each anatomical landmark j can be parameterized by its corresponding trajectory $\vec{a^j}$ over a full cardiac cycle. For a given volume sequence $I(t)$, one trajectory $\vec{a^j}$ is composed by the concatenation of the spatial coordinates:

$$\vec{a^j} = [\vec{a^j}(0), \vec{a^j}(1), \cdots, \vec{a^j}(t), \cdots, \vec{a^j}(n-1)] \qquad (2)$$

where $\vec{a^j}$ are spatial coordinates with $\vec{a^j}(t) \in \mathbb{R}^3$ and t an equidistant discrete time variable $t = 0, \cdots, n-1$.

The anatomical landmarks are also used to describe the global location and rigid motion, defined in Sec. III-A, as follows: $(c_x, c_y, c_z)_{aortic}$ ***equals to the gravity center of the aortic landmarks, except aortic leaflet tips.*** $\vec{\alpha}_z$ ***is the normal vector to the LR-Comm, NL-Comm, RN-Comm plane,*** $\vec{\alpha}_x$ ***is the unit vector orthogonal to*** $\vec{\alpha}_z$ ***which points from*** $(c_x, c_y, c_z)_{aortic}$ ***to LR-Comm,*** $\vec{\alpha}_y$ ***is the cross-product of*** $\vec{\alpha}_x$ ***and*** $\vec{\alpha}_z$. $(s_x, s_y, s_z)_{aortic}$ ***is given by the maximal distance between the center*** $(c_x, c_y, c_z)_{aortic}$ ***and the aortic landmarks, along each axes*** $(\vec{\alpha}_x, \vec{\alpha}_y, \vec{\alpha}_z)$. ***Analogously to the aortic valve, the barycentric position*** $(c_x, c_y, c_z)_{mitral}$ ***is computed from the mitral landmarks, except mitral leaflet tips.*** $\vec{\alpha}_z$ ***is the normal vector to the L/R-Trigone, PostAnn MidPoint plane,*** $\vec{\alpha}_x$ ***is orthogonal to*** $\vec{\alpha}_z$ ***and points from***
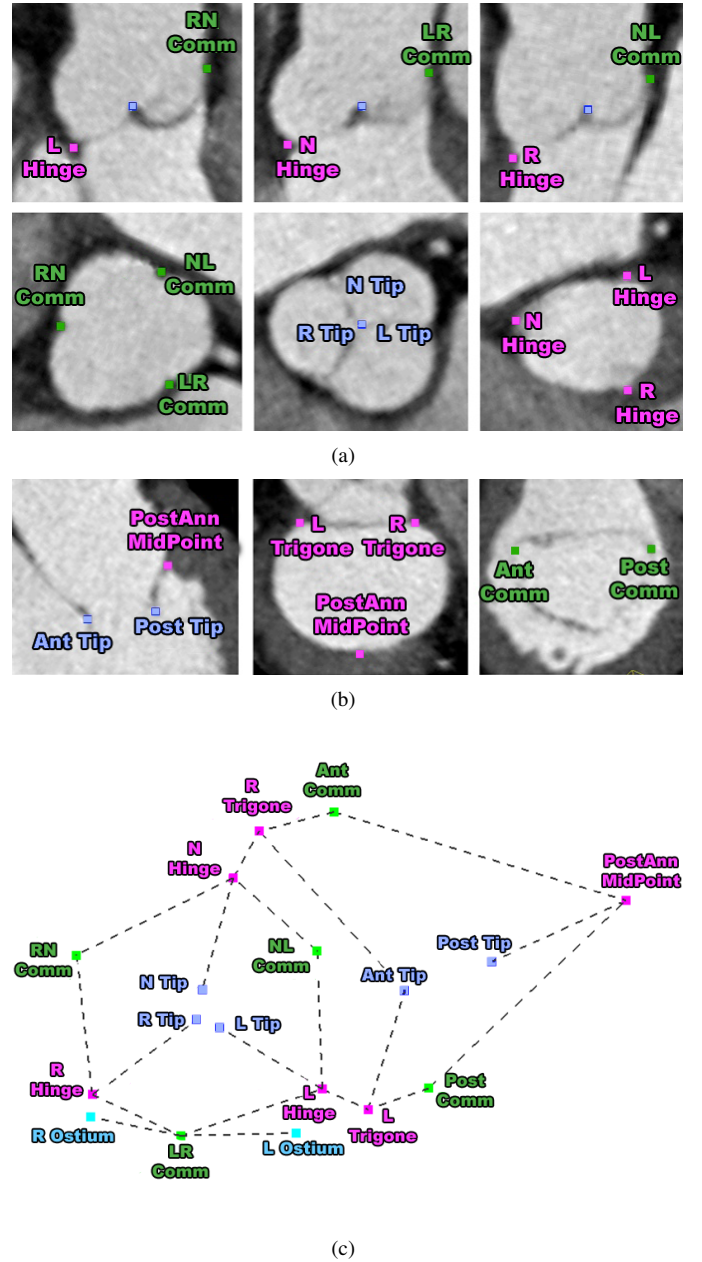

Fig. 3. Anatomical landmarks of the aorto-mitral complex: (a) aortic and (b) mitral landmarks in short and long axis views, and (c) complete landmark model (See Fig. 4 for a illustration of the landmarks relation to the comprehensive aortic-mitral model).

$(c_x, c_y, c_z)_{mitral}$ ***towards the PostAnn MidPoint. The scale parameters*** $(s_x, s_y, s_z)_{mitral}$ ***are defined as for the aortic valve, to comprise the entire mitral anatomy.***

C. Comprehensive Aortic-Mitral Model

The full geometry of the valves is modeled using surface meshes constructed along rectangular grids of vertices. For each anatomic structure a, the underlying grid is spanned along two physiologically aligned parametric directions, $\vec{u}$ and $\vec{v}$. Each vertex $\vec{v_i^a} \in \mathbb{R}^3$ has four neighbors, except the edge and corner points with three and two neighbors, respectively. ***Therefore, a rectangular grid with*** $n \times m$ ***vertices is represented by*** $(n-1) \times (m-1) \times 2$ ***triangular***
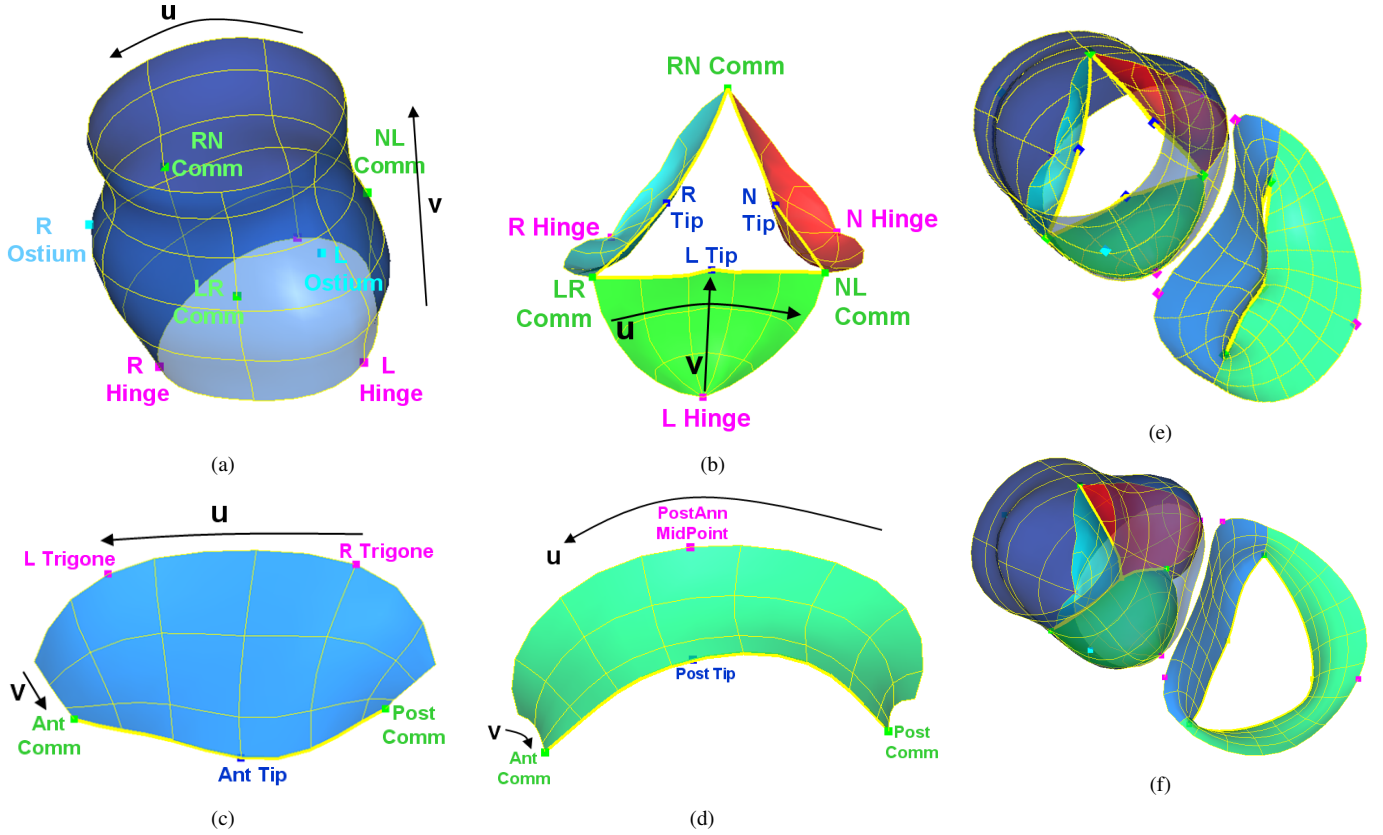
Fig. 4. Isolated surface components with parametric directions and spatial relations to anatomical landmarks: (a) aortic root and (b) leaflets, mitral (c) anterior and (d) posterior leaflet. Components all together in two different cardiac phases with (e) aortic valve and opened mitral valve closed and (f) vice versa. Aortic L-, R- and N-leaflets displayed in green, cyan and red color respectively.

faces. The model M at a particular time step t is uniquely defined by vertex collections of the anatomic structures. The time parameter t extends the representation to capture valve dynamics:

$$M = [\underbrace{\left\{v_0^{\vec{a}_1}, \cdots, v_{N_1}^{\vec{a}_1}\right\}}_{\text{first anatomy}}, \cdots, \underbrace{\left\{v_0^{\vec{a}_n}, \cdots, v_{N_n}^{\vec{a}_n}\right\}}_{\text{n-th anatomy}}, t] \qquad (3)$$

where $n = 6$ is the number of represented anatomies and $N_1 \ldots N_n$ are the numbers of vertices for a particular anatomy. The six represented structures are the aortic root, the three aortic leaflets and the two mitral leaflets, which are depicted in Fig. 4 together with their spatial relations to the anatomical landmarks.

The aortic root connects the ascending aorta to the left ventricle outflow tract and is represented through a tubular grid (Fig. 4(a)). This is aligned with the aortic circumferential u and ascending directions v and includes 36×20 vertices and 1368 faces. The root is constrained by six anatomical landmarks, i.e., three commissures and three hinges, with a fixed correspondence on the grid. The three aortic leaflets, the L-, R- and N-leaflet, modeled as paraboloids on a grid of 11×7 vertices and 120 faces (Fig. 4(b)). They are stitched to the root on a crown like attachment ring, which defines the parametric u direction at the borders. The vertex correspondence between the root and leaflets along the

merging curve is symmetric and kept fixed. The leaflets are constrained by the corresponding hinges, commissures and tip landmarks, where the v direction is the ascending vector from the hinge to the tip.

The mitral leaflets separate the LA and LV hemodynamically and are connected to the endocardial wall by the saddle shaped mitral annulus. Both are modeled as paraboloids and their upper margins define the annulus implicitly. Their grids are aligned with the circumferential annulus direction u and the orthogonal direction v pointing from the annulus toward leaflet tips and commissures (Fig. 4(c) and 4(d)). The anterior leaflet is constructed from 18×9 vertices and 272 faces while the posterior leaflet is represented with 24×9 vertices and 368 faces. Both leaflets are fixed by the mitral commissures and their corresponding leaflet tips. The left / right trigones and the postero-annular midpoint further confine the anterior and posterior leaflets, respectively.

D. Maintaining Spatial and Temporal Consistency

Point correspondence between the models from different cardiac phases and across patients is required for building a statistical shape model (applied in Sec. IV-C). It is difficult to obtain and maintain a consistent parameterization as presented in Sec. III-C in complex three-dimensional surfaces. However, cutting planes can be applied to intersect surfaces (Fig. 5(b), 5(c) and 5(d)) and generate two-dimensional contours (Fig.
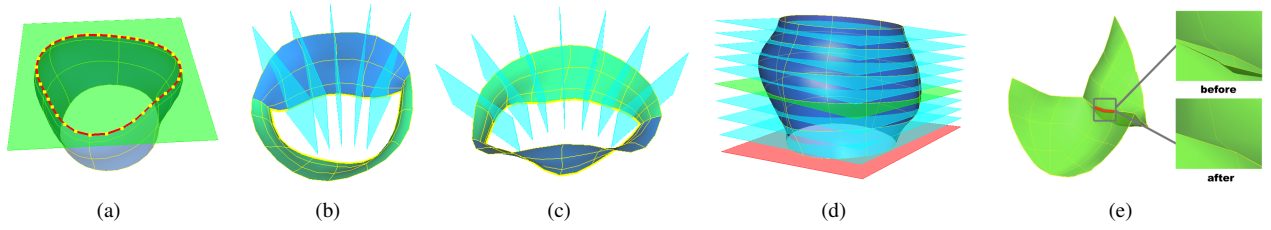
Fig. 5. (a) Example of a two-dimensional contour and corresponding uniform samples, obtained from the intersection of a plane with the three-dimensional aortic root. Resampling planes for the mitral leaflets (b,c) and aortic root (d). The planes at the hinge and commissure levels of the aortic root in (d) are depicted in red and green respectively. Note that for the purpose of clarity only a subset of resampling planes is visualized in figs (b),(c) and (d). (e) Leaflet closure line correction.

5(a)), which can be uniformly resampled using simple methods. Hence, by defining a set of physiological-based cutting planes for each model component, surfaces are consistently resampled to establish the desired point correspondence.

As mentioned in Sec. III-C the mitral annulus is a saddle shaped curve and likewise the free edges are non-planar too. Thus a rotation axis based resampling method is applied for both mitral leaflets (Fig. 5(b) and 5(c)). The intersection planes pass through the annular midpoints of the opposite leaflet. They are rotated around the normal of the plane spanned by the commissures and the respectively used annular midpoint.

For the aortic root (Fig. 5(d)) a pseudo parallel slice based method is used. Cutting planes are equidistantly distributed along the centerline following the v direction. To account for the bending of the aortic root, especially between the commissure and hinge level, at each location the plane normal is aligned with the centerline's tangent. For the aortic leaflets, resampling of the iso-curves along their u and v directions is found to be sufficient.

The anatomical constraints prevent leaflet intersection, during valve closure, when leaflets are touching each other to form the leaflet-coaptation area. Potential numerical errors, which can accumulate at a small scale causing leaflet intersection along the closure line, can be efficiently handled using a simple post-processing. Given the point correspondence preserved by the model, averaging adjacent points within the intersection area restores model consistency and ensure high quality visualization as illustrated in Fig. 5(e).

IV. PATIENT-SPECIFIC AORTIC-MITRAL MODEL ESTIMATION

The model parameters introduced in Sec. III are estimated from volumetric sequences (3D+time data), to construct patient-specific aortic-mitral representations. We introduce a robust learning-based algorithm, which in concordance with the hierarchical parameterization includes three stages: global location and rigid motion estimation, non-rigid landmark motion estimation and comprehensive aortic-mitral estimation. Fig. 6 illustrates the entire algorithm, which relies on novel techniques such as the trajectory spectrum learning (TSL) with local-spatio-temporal (LST) features [6] and extends recent machine learning methods [10], [33]. *Please note that in practice, the same framework is used for the two imaging modalities without any modification in the algorithms, but detectors that estimate the probabilities of model parameters are learned separately for CT and TEE data.*

A. Global Location and Rigid Motion Estimation

The location and motion parameters θ, defined in Sec. III-A, are estimated using the Marginal Space Learning (MSL) framework [10] in combination with Random Sample Consensus (RANSAC) [34]. Given a sequence of volumes I, the task is to find similarity parameters θ with maximum posterior probability:

$$\arg\max_\theta p(\theta|I) = \arg\max_\theta \\ p(\theta(0), \cdots, \theta(n-1)|I(0), \cdots, I(n-1)) \quad (4)$$

To solve equation 4, we formulate the object localization as a classification problem and estimate $\theta(t)$ for each time step t independently, from the corresponding volumes $I(t)$. The probability $p(\theta(t)|I(t))$ is modeled by a learned detector D, which evaluates and scores a large number of hypotheses for $\theta(t)$. D is trained using the Probabilistic Boosting Tree (PBT) [33], positive and negative samples extracted from the ground-truth, as well as efficient 3D Haar wavelet [35] and steerable features [10].

The object localization task is performed by scanning the trained detector D exhaustively over all hypotheses to find the most plausible values for $\theta(t)$ at each time step t. As the number of hypotheses to be tested increases exponentially with the dimensionality of the search space, a sequential scan in a nine-dimensional, similarity transform, space is computationally unfeasible. Suppose each dimension in $\theta(t)$ is discretized to n values, the total number of hypotheses is n^9 and even for a small $n = 15$ becomes extreme 3.98^{e+10}. To overcome this limitation, we apply the MSL framework, which breaks the original parameters space Σ into subsets of increasing marginal spaces:

$$\Sigma_1 \subset \Sigma_2 \subset \cdots \subset \Sigma_n = \Sigma$$

By decomposing the original search space as follows (*please refer to Sec. III-A for a complete descriptions of the parameters*)

$$\begin{aligned} \Sigma_1 &= (c_x, c_y, c_z) \\ \Sigma_2 &= (c_x, c_y, c_z, \vec{\alpha}_x, \vec{\alpha}_y, \vec{\alpha}_z) \\ \Sigma_3 &= (c_x, c_y, c_z, \vec{\alpha}_x, \vec{\alpha}_y, \vec{\alpha}_z, s_x, s_y, s_z) \end{aligned}$$
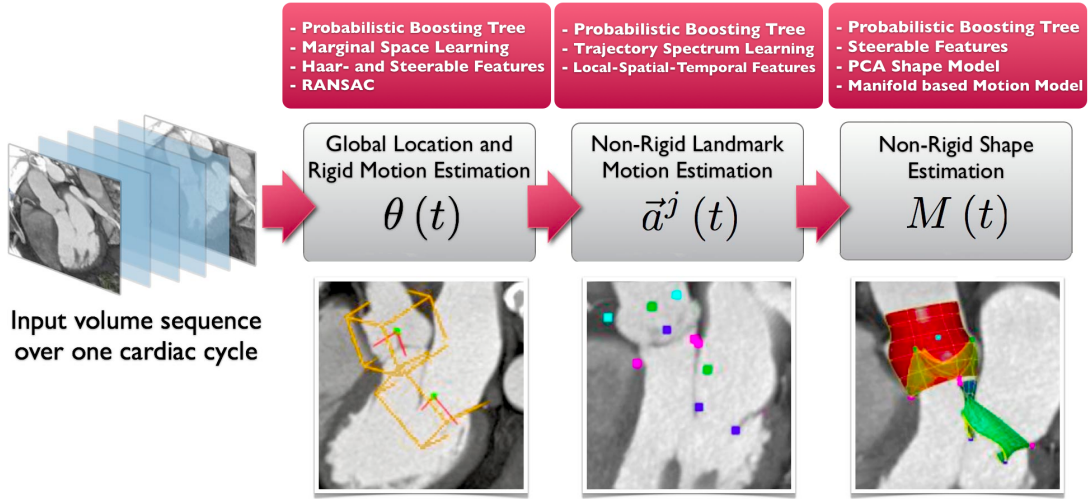
Fig. 6. Diagram depicting the hierarchical model estimation algorithm. Each block describes the actual estimation stage, computed model parameters and underlying approach.

the target posterior probability can be expressed as:

$$p(\theta(t)|I(t)) = p(c_x, c_y, c_z|I(t))$$
$$p(\vec{\alpha}_x, \vec{\alpha}_y, \vec{\alpha}_z|c_x, c_y, c_z, I(t))$$
$$p(s_x, s_y, s_z|\vec{\alpha}_x, \vec{\alpha}_y, \vec{\alpha}_z, c_x, c_y, c_z, I(t))$$

In practice, the optimal arrangement for MSL sorts the marginal spaces in a descending order based on their variance. Learning parameters with low variance first will decrease the overall precision of the detection. In our case, due to CT and TEE acquisition protocols and physiological variations of the heart, the highest variance comes from translation followed by orientation and scale. This order is confirmed by our experiments to output the best results.

Instead of using a single detector D, we train detectors for each marginal space (D_1, D_2 and D_3) and detect by gradually increasing dimensionality. After each stage only a limited number of high-probability candidates are kept to significantly reduce the search space. *Experimentally determined as in [10], 100 highest score candidates are retained in Σ_1, 50 in Σ_2 and 25 in Σ_3, such that the smallest subgroup which is likely to include the optimal solution is preserved.*

The candidates with the highest score, $[\theta^0(0)\ldots\theta^{25}(0)]\ldots[\theta^0(n-1)\ldots\theta^{25}(n-1)]$, estimated at each time step t, $t = 0, \ldots n-1$ are aggregated to obtain a temporal consistent global location and motion $\theta(t)$ by employing a RANSAC estimator. From randomly sampled candidates, the one yielding the maximum number of inliers is picked as the final motion. Inliers are considered within a distance of $\sigma = 7mm$ from the current candidate and extracted at each time step t. The distance measure $d(\theta(t)_1, \theta(t)_2)$ is given by the maximum L1 norm of the standard unit axis deformed by the parameters $\theta(t)_1$ and $\theta(t)_2$, respectively. The resulting time-coherent $\theta(t)$ describes the global location and rigid motion over the entire cardiac cycle.

B. Non-rigid Landmark Motion Estimation

Based on the determined global location and rigid motion, in this section we introduce a novel trajectory spectrum learning algorithm to estimate the non-linear valve movements from volumetric sequences. Considering the representation in section III-B equation 2, the objective is to find for each landmark j its trajectory $\vec{a^j}$, with the maximum posterior probability from a series of volumes I, **given the rigid motion θ**:

$$\arg\max_{\vec{a^j}} p(\vec{a^j}|I, \theta) = \arg\max_{\vec{a^j}} p(\vec{a^j}(0), \cdots, \vec{a^j}(n-1)|$$
$$I(0), \cdots, I(n-1), \theta(0), \cdots, \theta(n-1)) \quad (5)$$

Note that Equ. 5 only models the non-rigid landmark motion, as the global location and motion is removed from the trajectories by aligning $\vec{a^j}, j = 0 \ldots 10$ with the aortic and $\vec{a^j}, j = 11 \ldots 17$ with the mitral similarity parameters θ estimated as described in Sec. IV-A. While it is difficult to solve equation 5 directly, various assumptions, such as the Markovian property of the motion [36], have been proposed to the posterior distribution over $\vec{a^j}(t)$ given images up to time t. However, results are often not guaranteed to be smooth and may diverge over time, due to error accumulation. These fundamental issues can be addressed effectively if both, temporal and spatial appearance information, is considered over the whole sequence at once.

The trajectory representation $\vec{a^j}$ introduced in equation 2 can be uniquely represented by the concatenation of its discrete Fourier transform (DFT) coefficients,

$$\vec{s^j} = [\vec{s^j}(0), \vec{s^j}(1), \cdots, \vec{s^j}(n-1)] \quad (6)$$

obtained through the DFT equation:

$$\vec{s^j}(f) = \sum_{t=0}^{n-1} \vec{a^j}(t) e^{\frac{-j2\pi t f}{n}}$$

where $\vec{s^j}(f) \in \mathbb{C}^3$ is the frequency spectrum of the x, y, and z components of the trajectory $\vec{a^j}(t)$, and $f = 0, 1, \cdots, n-1$
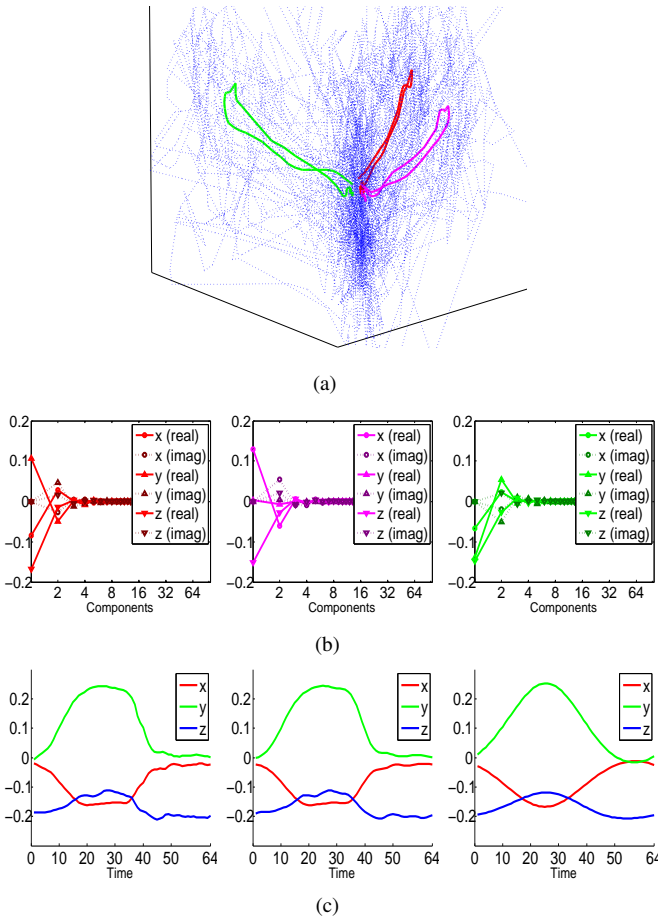
(a)

(b)

(c)

Fig. 7. *Example trajectories of aortic leaflet tips. (a) the aligned trajectories in the Cartesian space by removing the global similarity transformations. (b) corresponding 3 trajectories highlighted in red, magenta and green, which demonstrates the compact spectrum representation. (c) Reconstructed trajectories of using 64, 10, and 3 components, respectively, showing that a small number of components can be used to reconstruct faithful motion trajectories. The vertical axis represents the normalized motion magnitude with respect to the reference bounding box as illustrated in Fig. 2.*

(see Fig. 7). A trajectory $\vec{a^j}$ can be exactly reconstructed from the spectral coefficients $\vec{s^j}$ applying the inverse DFT:

$$\vec{a^j}(t) = \sum_{f=0}^{n-1} \vec{s^j}(f) e^{\frac{j2\pi tf}{n}} \qquad (7)$$

The estimated trajectory is obtained using the magnitude of the inverse DFT. From the DFT parameterization the equation 5 can be reformulated as finding the DFT spectrum $\vec{s^j}$, with maximal posterior probability:

$$\arg\max_{\vec{s^j}} p(\vec{s^j}|I,\theta) = \arg\max_{\vec{s^j}} p(\vec{s^j}(0), \cdots, \vec{s^j}(n-1)| \\ I(0), \cdots, I(n-1), \theta(0), \cdots, \theta(n-1)) \qquad (8)$$

Instead of estimating the motion trajectory directly, we apply discriminative learning to detect the spectrum $\vec{s^j}$ in the frequency domain by optimizing equation 8. The proposed formulation benefits from three qualities:

- the DFT decomposes the trajectory space in **orthogonal subspaces**, which enables the estimation of each component $\vec{s^j}(f)$ separately.
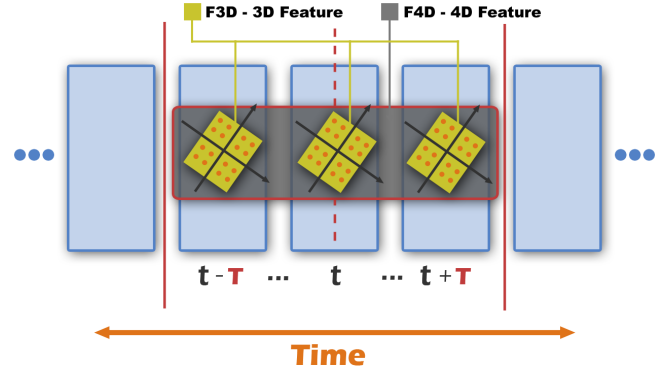

Fig. 9. An example of a local-spatio-temporal feature, align with a certain position, orientation and scale, at time t. The temporal context length of the illustrated LST feature is T, spanned symmetrical relative to t.

- the DFT spectrum **representation is compact**, especially for periodic motion allowing for efficient learning and optimization.
- the **posterior distribution is clustered** in small regions facilitating marginalization and pruning of the higher dimensional parameter spaces.

Inspired by the MSL reviewed in Section IV-A, we efficiently perform trajectory spectrum learning and detection in DFT subspaces with gradually increased dimensionality. The intuition is to perform a spectral coarse-to-fine motion estimation, where the detection of coarse level motion (low frequency) is incrementally refined with high frequency components representing fine deformations. Section IV-B.1 presents our novel Local-Spatio-Temporal (LST) features to incorporate both the spatial and temporal context. The space marginalization and training procedure of our trajectory estimator is introduced in Section IV-B.2. Section IV-B.3 illustrates the application of the learned detector for motion estimation from unseen data. The trajectory spectrum learning algorithm is summarized in Fig. 8.

1) Local-Spatio-Temporal Features: It has been shown that local orientation and scaling of image features reduce ambiguity and significantly improves learning performance [37]. We extend the image representation by aligning contextual spatial features in time, to capture four-dimensional information and support motion learning from noisy data. The 4D location of the proposed $F^{4D}()$ features is parameterized by the similarity parameters θ, defined in Sec. III-A and estimated in IV-A:

$$F^{4D}(\theta(t), T|I, s) = \\ \tau(F^{3D}(I, \theta(t + i * s)), i = -T, \cdots, T) \qquad (9)$$

Three-dimensional $F^{3D}()$ features extract simple gradient and intensity information from steerable pattern spatially align with $\theta(t)$ (see [10] for the exact definition). ***Please note that according to the anatomical structure, the similarity parameters θ are defined separately for the aortic and mitral valves (see Sec. III-B).*** Knowing that motion is locally coherent in time, $F^{3D}()$ is applied in a temporal neighborhood $t - T$ to $t + T$ at discrete locations evenly distributed with respect to the current time t (see Fig. 9). The final value
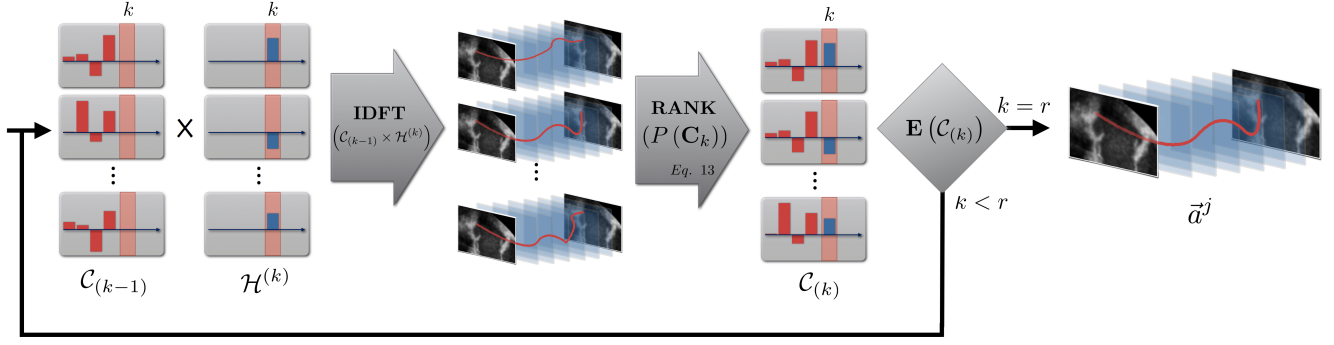
Fig. 8.   Diagram depicting the estimation of non-rigid landmark motion using trajectory spectrum learning.

of a Local-Spatial-Temporal (LST) feature is the result of time integration using a set of linear kernels τ, which weight spatial features $F^{3D}()$ according to their distance from the current frame t. **A simple example for τ, also used in our implementation, is the uniform kernel over the interval $[-T, T]$, $\tau = 1/(2T+1)\sum_{i=-T}^{T}(F^{3D}(I, \theta(t + i * s))$. For this choice of τ, each F^{3D} contributes equally to the F^{4D}.**

The parameter T steers the size of the temporal context, while s is a time normalization factor derived from the training set and the number of time steps of the volume sequence I. Values for T can be selected by the probabilistic boosting tree (PBT) [33] in the training stage. Since the time window size has an inverse relationship with the motion locality, the introduced 4D local features are in consensus with a coarse-to-fine search. Our experimental results support this property by showing that the features with larger T values are selected to capture the lower frequency motion, and the value of T decreases for higher frequency motion components.

2) Learning in Marginal Trajectory Spaces: As described earlier, the motion trajectory is parameterized by the DFT spectrum components $\vec{s}^j(f), f = 0, \ldots, n-1$. Fig. 7 clearly shows that the variation of the spectrum components decreases substantially as the frequency increases. Consequently, trajectories can be adequately approximated by a few dominant components:

$$\zeta \subseteq \{0, \ldots, n-1\}, |\zeta| << n$$

identified during training. The obtained compact search space can be divided in a set of subspaces. We differentiate between two types of subspaces, individual component subspaces $\Sigma^{(k)}$ and marginalized subspaces Σ_k defined as:

$$\Sigma^{(k)} = \{\vec{s}(k)\} \tag{10}$$
$$\Sigma_k = \Sigma_{k-1} \times \Sigma^{(k)} \tag{11}$$
$$\Sigma_0 \subset \Sigma_1 \subset \ldots \subset \Sigma_{r-1}, r = |\zeta| \tag{12}$$

The subspaces $\Sigma^{(k)}$ are efficiently represented by a set of corresponding hypotheses $H^{(k)}$ obtained from the training set. The pruned search space enables efficient learning and optimization:

$$\Sigma_{r-1} = \mathcal{H}^{(0)} \times \mathcal{H}^{(1)} \times \ldots \times \mathcal{H}^{(r-1)}, r = |\zeta|$$

The training algorithm starts by learning the posterior probability distribution in the DC marginal space Σ_0. Subsequently, the learned detectors D_0 is applied to identify high probable candidates $\mathcal{C}_0$ from the hypotheses $\mathcal{H}^{(0)}$. In the following step, the dimensionality of the space is increased by adding the next spectrum component (in this case the fundamental frequency, $\Sigma^{(1)}$). Learning is performed in the restricted space defined by the extracted high probability regions and hypotheses set $\mathcal{C}_0 \times \mathcal{H}^{(1)}$. The same operation is repeated until reaching the genuine search space Σ_{r-1}.

For each marginal space Σ_k, corresponding discriminative classifiers D_k are trained on sets of positives Pos_k and negatives Neg_k. We analyze samples constructed from high probability candidates $\mathcal{C}_{k-1}$ and hypotheses $\mathcal{H}^{(k)}$. The sample set $\mathcal{C}_{k-1} \times \mathcal{H}^{(k)}$ is separated into positive and negative examples by comparing the corresponding trajectories to the ground truth in the spatial domain using the following distance measure:

$$d(\vec{a^j}_1, \vec{a^j}_2) = \max_t \|\vec{a^j}_1(t) - \vec{a^j}_2(t)\|$$

where $\vec{a^j}_1$ and $\vec{a^j}_2$ denote two trajectories for the j-th landmark. It is important to note that the ground truth spectrum is trimmed to the $k-th$ component to match the dimensionality of the current marginal space Σ_k. Given the local-spatio-temporal features extracted from positive and negative positions, the probabilistic boosting tree (PBT) is applied to train a strong classifier D_k. The above procedure is repeated, increasing the search space dimensionality in each step, until detectors are trained for all marginal spaces $\Sigma_0, \ldots, \Sigma_{r-1}$.

3) Motion Trajectory Estimation: In this section we describe the detection procedure for object localization and motion estimation of valve landmarks from unseen volumetric sequences. The parameter estimation is conducted in the marginalized search spaces $\Sigma_0, \ldots, \Sigma_{r-1}$ using the trained spectrum detectors $D_0, \ldots, D_{r-1}$ (see Section IV-B.2). Starting from an initial zero-spectrum, we incrementally estimate the magnitude and phase of each frequency component $\vec{s}(k)$. At the stage k, the corresponding robust classifier D_k is exhaustively scanned over the potential candidates $\mathcal{C}_{k-1} \times \mathcal{H}^{(k)}$.
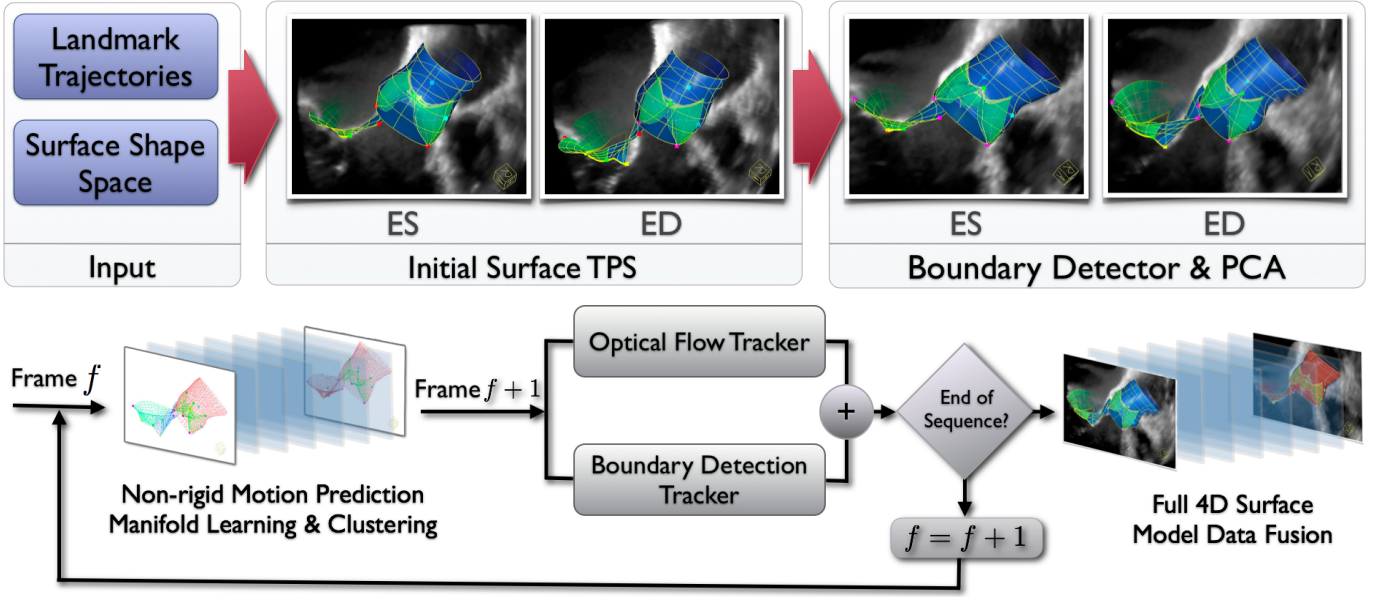
Fig. 10. Diagram depicting the estimation of the comprehensive aortic-mitral estimation. (top) model estimation in cardiac key phases, end-diastole and end-systole. (bottom) estimation in the full cardiac cycle.

The probability of a candidate $C_k \in \mathcal{C}_{k-1} \times \mathcal{H}^{(k)}$ is computed by the following objective function (see Fig. 8):

$$p(C_k) = \prod_{t=0}^{n-1} D_k(IDFT(C_k), I, t) \qquad (13)$$

where $t = 0, \ldots, n-1$ is the time instance (frame index). After each step k, the top 50 trajectory candidates $\mathcal{C}_k$ with high probability values are preserved for the next step $k+1$. The set of potential candidates $\mathcal{C}_{k+1}$ is constructed from the cross product of the candidates $\mathcal{C}_k$ and $\mathcal{H}^{(k+1)}$. The procedure is repeated until a final set of trajectory candidates $\mathcal{C}_{r-1}$, defined in the full space Σ_{r-1}, is computed. The final trajectory is reported as the average of all elements in $\mathcal{C}_{r-1}$.

C. Comprehensive Aortic-Mitral Estimation

The final stage in our hierarchical model estimation algorithm is the delineation of the full dynamic morphology of the aortic-mitral complex. The shape model is first estimated in the end-diastolic (ED) and end-systolic (ES) phases of the cardiac cycle. Then the non-rigid deformation is propagated to the remaining phases using a learned motion prior. Fig. 10 summarizes the steps for non-rigid shape estimation.

1) Estimation in Cardiac Key Phases: Given the previously detected anatomical landmarks in the ED and ES phases, a precomputed mean model of the anatomy is placed into the volumes $I(t_{ED})$ and $I(t_{ES})$ through a thin-plate-spline (TPS) transform [38]. In order to provide a locally accurate model estimate, a learning-based 3D boundary detection is then applied to deforming the shape to capture the anatomical and pathological variations (see Fig. 10 (top)).

We have shown that learning based methods provide better results [10], [36], when utilizing both gradients and image intensities at different image resolutions and by incorporating local neighborhood. Therefore the boundary detector is trained

using the probabilistic boosting-tree (PBT) on multi-scale steerable features [10]. In the testing stage, the boundary detector is used to evaluate a set of hypotheses, which are drawn along the normal at each of the discrete boundary points. The new boundary points are set to the hypotheses with maximal probability. The final model is obtained after projecting the estimated points to a principal component analysis (PCA) space. ***In order to determine the dimension of the subspace, the cumulated variation $v(m)$ for the first m modes was computed from the eigenvalues λ_i as follows: $v(m) = \sum_{i=1}^{m} \lambda_i / \sum_{i=1}^{N} \lambda_i$ [19]. Fig. 11 depicts the fraction $v(m)$ for the shapes of the aortic and mitral valve respectively. By demanding the subspace to cover 99.5% of the shape variation we determined the number of necessary modes as 72 and 98 respectively.***
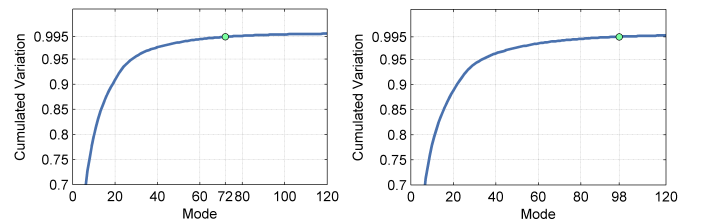

Fig. 11. Cumulated shape variation for (a) aortic and (b) mitral valves. The green dot marks the threshold cumulated variance of 0.995.

2) Motion Estimation: Starting from the detection results in the ED and ES phases, the model deformations are propagated in both forward and backward directions using learned motion priors similar as in [36] (Fig. 10 (bottom)). The motion prior is estimated at the training stage using motion manifold learning and hierarchical K-means clustering, from a pre-annotated database of sequences containing one cardiac cycle each. Firstly the temporal deformations are aligned by 4D generalized procrustes analysis. Next a low-dimensional

embedding is computed from the aligned training sequences using the ISOMAP algorithm [39], to represent the highly nonlinear motion of the heart valves. Finally, in order to extract the modes of motion, the motion sequences are then clustered with hierarchical K-means based on the Euclidean distance in the lower dimensional manifold.

To ensure temporal consistency and smooth motion and to avoid drifting and outliers, two collaborative trackers, an optical flow tracker and a boundary detection tracker, are used in our method. The optical flow tracker directly computes the temporal displacement for each point from one frame to the next. Initialized by one-step forward prediction, the detection tracker obtains the deformations in each frame with maximal probability. The results are then fused into a single estimate by averaging the computed deformations and the procedure is repeated until the full 4D model is estimated for the complete sequence. In this way the collaborative trackers complement each other, as the optical flow tracker provides temporally consistent results and its major issue of drifting is addressed by the boundary detection along with the one-step forward prediction.

V. MODEL-BASED QUANTIFICATION OF THE AORTIC-MITRAL APPARATUS

From the estimated patient-specific model we efficiently derive a wide-ranging morphological and functional characterization of the aortic-mitral apparatus, summarized in Tab. I. In comparison with the gold standard, which processes 2D images and performs manual measurements, the benefits of the proposed automatic quantization are:

- **Precision** increased by modeling and measuring the natural three-dimensional valve anatomy.
- **Reproducibility** through automatic quantification and avoidance of user-dependent manipulation.
- **Functional** assessment from dynamic measurements performed over the entire cardiac-cycle.
- **Comprehensive** analysis including complex parameters such as shape curvatures, deformation fields and volumetric variations.

Comprehensive valve measurements are important in the clinical workflow during diagnosis and severity assessment, surgery planning for replacement or repair and percutaneous interventions [2]. Valvular dimensions, such as Aortic Valve Area, Mitral valve Area and Mitral Annulus Area (Fig. 12), automatically obtained over the whole cardiac cycle, can benefit cardiologists in evaluating the overall structural and functional condition. Furthermore, in-depth analysis of complex pathologies can be performed through independent Sinus Volumes quantization and Annular Deviation assessment for the aortic and mitral valves, respectively.

Dimensions of the aortic root at the Ventriculoarterial Junction, Valsalva Sinuses and Sinotubular Junction as well as the Inter-ostia angle are crucial in planning for aortic valve replacement and repair surgery [44]. These, along with measurements of the mitral annulus and leaflets, such as the mitral Annular circumference, Anterolateral-Posteromedial diameter, can be automatically computed by the proposed approach (see Fig.12)

TABLE I
AORTIC-MITRAL MEASUREMENTS, AUTOMATICALLY COMPUTED FROM THE PATIENT-SPECIFIC MODEL OVER THE ENTIRE CARDIAC CYCLE

Aortic Root	**Mitral Annulus**
Ventriculoarterial Junct. $\oslash,\int,\vee$ [18]	Annular $\int,\vee$ [2], [18]
Valsava Sinuses $\oslash,\int,\vee$ [18]	Annular Deviation Ratio [41]
Sinotubular Junct. $\oslash,\int,\vee$ [18]	Annular Non-Planarity $\angle$ [17]
Commissure-Hinge Plane $\angle$	Sphericity Index
Sinus Volumes	
Aortic Landmarks	**Mitral Landmarks**
Commissure-Hinge Distance [18]	Inter-Commissural Distance [2]
Hinge-Ostium Distance [40]	Inter-Trigonal Distance [2]
Ostium-Commissure Distance	Annular-Posterior $\oslash$ [2]
Inter-Commissural $\vee,\angle$ [18]	Anterolateral-Posteromedial $\oslash$ [2]
Inter-Ostia $\angle$	Annular-Commissural Ratio [42]
Aortic Leaflets	**Mitral Leaflets**
Aortic Valve $\int$ [40]	Anterior/Posterior Surface $\int,\vee$
Coaptation Height [18]	Valve Opening $\int$ [2]
Leaflet Height [40]	Valve to Area Ratio
Effective Cusp Height [40]	Tenting Height and Volume [2], [43]
Leaflet Free Edge $\vee$ [40]	
Leaflet-Ostium Distance	**Aortic-Mitral**
	Centroid Distances [18]
	Inter-Annular $\angle$ [18]

$\oslash$ - diameter, $\int$ - area, $\vee$ - circumferential length, $\angle$ - angle.

Emerging percutaneous and minimally invasive valve interventions require extensive non-invasive assessment and can substantially benefit from the model-based quantification [40]. For instance, precise knowledge of the coronary ostia position prevents hazardous ischemic complications by avoiding the potential misplacement of aortic valve implants. The method presents an integral three-dimensional configuration of critical structures (ostia, commissures, hinges, etc.) and calculates their relative location over the entire cardiac cycle. Additionally, the joint model characterizes the aortic-mitral interconnection by quantifying the Inter-Annular angle and Centroid Distances (Fig. 12), which facilitates the challenging management of multi-morbid patients.

It is important to notice, that the quantification potential of the proposed method is not limited to the above mentioned measurements. Through the consistent and comprehensive spatial and temporal representation, the introduced system offers unique analysis features, which facilitate decisions during the whole clinical workflow. For the first time, functional and morphological measurements can be efficiently performed for individual valve patients and potentially improve their clinical management.

VI. EXPERIMENTS

In this section, we demonstrate the performance of the proposed patient-specific modeling and quantification method for aortic and mitral valves. Experiments are performed on a large and comprehensive data set described in Section VI-A. In section VI-B, we demonstrate the performance of the model estimation algorithm on cardiac CT and TEE volumetric sequences. The clinical evaluation in VI-C presents the quantification performance and accuracy for the proposed system.

A. Data Set

Functional cardiac studies were acquired using CT and TEE scanners from 134 patients affected by various car-
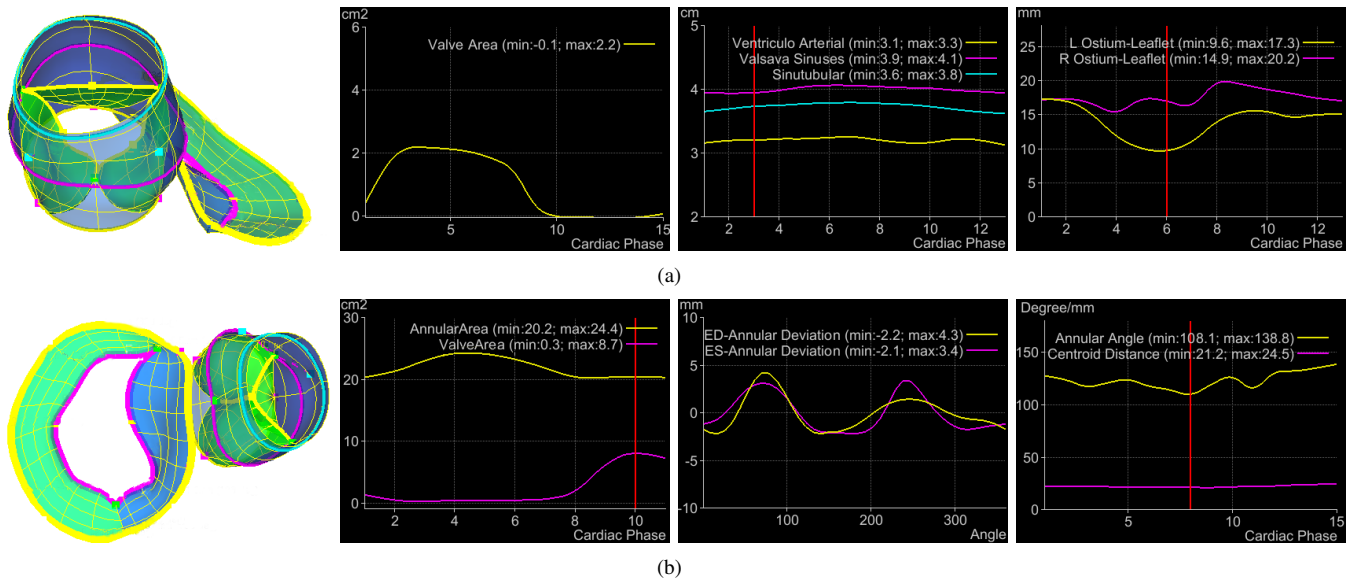
Fig. 12. Examples of aortic-mitral morphological and functional measurements. (a) from left to right: aortic valve model with measurement traces, aortic valve area, aortic root diameters and ostia to leaflets distances. (b) mitral valve with measurement traces, mitral valve and annulus area, mitral annular deviation in ED and ES and aortic-mitral angle and centroid distance.

diovascular diseases such as: bicuspid aortic valve, dilated aortic root, stenotic aortic/mitral, regurgitant aortic/mitral as well as prolapsed valves. The imaging data includes 690 CT and 1516 TEE volumes, which were collected from medical centers around the world over a period of two years. Using heterogeneous imaging protocols, TEE exams were performed with Siemens Acuson Sequoia (Mountain View, CA, USA) and Philips IE33 (Andover, MA, USA) ultrasound machines while CT scans were acquired using Siemens Somatom Sensation or Definition scanners (Forchheim, Germany). The ECG gated Cardiac CT sequences include 10 volumes per cardiac cycle, where each volume contains 80-350 slices with 153×153 to 512×512 pixels. The in-slice resolution is isotropic and varies between 0.28 to 1.00mm with a slice thickness from 0.4 to 2.0mm. TEE data includes an equal amount of rotational (3 to 5 degrees) and matrix array acquisitions. A complete cardiac cycle is captured in a series of 7 to 39 volumes, depending on the patient's heart beat rate and scanning protocol. Image resolution and size varies for the TEE data set from 0.6 to 1 mm and $136 \times 128 \times 112$ to $160 \times 160 \times 120$ voxels, respectively.

The ground truth for training and testing was obtained through an annotation process, which was guided by experts and includes the following steps:

- *the non-rigid landmark motion model is manually determined by placing each anatomical landmark (Sec. III-B) at the correct location in the entire cardiac cycle of a given study.*
- *the comprehensive aortic-mitral model is initialized through its mean model placed at the correct image location, expressed by the thin-plate-spline transform estimated from the previously annotated non-rigid landmark motion model (see Sec. IV-C).*
- *the ground-truth of the comprehensive aortic-mitral model is manually adjusted to delineate the true valves boundary over the entire cardiac cycle.*
- *from the annotated non-rigid landmark motion model,*

the global location and rigid motion model ground-truth is determined as described in Sec. III-B.

Please note that while CT acquisitions contain both valves, it is not always the case for the TEE exams, which usually focus either on the aortic or mitral valve. Ten cases were annotated by four distinct user for the purpose of conducting inter-user variability study, which is presented in section VI-C. Also for a number of four patients we obtained both, CT and TEE studies, and used that for an inter-modality study also presented in section VI-C.

B. Model Estimation Performance

The precision of the global location and rigid motion estimation (Sec. IV-A) is measured at the box corners of the detected time-dependent similarity transformation. Hence, the average Euclidean distance between the eight bounding box points, defined by the similarity transform $(c_x, c_y, c_z), (\vec{\alpha}_x, \vec{\alpha}_y, \vec{\alpha}_z), (s_x, s_y, s_z)$, and the ground-truth box is reported. To measure the accuracy of the non-rigid landmark motion estimation (Sec. IV-B), detected and ground-truth trajectories of all landmarks are compared at each discrete time step using the Euclidean distance. The accuracy of the surface models obtained by the comprehensive aortic-mitral estimation (Sec. IV-C) is evaluated by utilizing the point-to-mesh distance. For each point on a surface (mesh), we search for the closest point (not necessarily one of the vertices) on the other surface to calculate the Euclidean distance. To guarantee a symmetric measurement, the point-to-mesh distance is calculated in two directions, from detected to ground truth surfaces and vice versa.

The performance evaluation was conducted using three-fold cross-validation by dividing the entire dataset into three equally sized subsets, and sequentially using two sets for training and one for testing. Table II summarizes the model estimation performance averaged over the three evaluation

runs. The last column represents the 80th percentile of the error values. The estimation accuracy averages at 1.54mm and 1.36mm for TEE and CT data, respectively. On a standard PC with a quad-core 3.2GHz processor and 2.0GB memory, the total computation time for the tree estimation stages is 4.8 seconds per volume (approx 120sec for average length volume sequences), *from which the global location and rigid motion estimation requires 15% of the computation time (approx 0.7sec), non-rigid landmark motion 54% (approx 2.6sec) and comprehensive aortic-mitral estimation 31% (approx 1.5sec).* Fig. 13 shows estimation results on various pathologies for both valves and imaging modalities.

TABLE II

ERRORS FOR EACH ESTIMATION STAGE IN TEE AND CT

TEE	Mean	Std.	Median	80%
Global Location and Rigid Motion	6.95	4.12	5.96	8.72
Non-Rigid Landmark Motion	3.78	1.55	3.43	4.85
Comprehensive Aortic-Mitral	1.54	1.17	1.16	1.78
CT	Mean	Std.	Median	80%
Global Location and Rigid Motion	8.09	3.32	7.57	10.4
Non-Rigid Landmark Motion	2.93	1.36	2.59	3.38
Comprehensive Aortic-Mitral	1.36	0.93	1.30	1.53

For the non-rigid landmark motion, we analyzed the error distribution of our approach and compared it to optical flow [45] and tracking-by-detection [46]. Fig. 14(a) presents the error distribution over the entire cardiac cycle, where the end-diastolic phase is at $t = 0$. It can be seen that, although performed forward and backward, the optical flow approach is affected by drifting. In the same time, the tracking-by-detection error is unevenly distributed, which reflects in temporal inconsistent and noisy results. Fig. 14(b) shows the error distribution over the 18 landmarks. Both tracking-by-detection and optical flow perform significantly worse on highly mobile landmarks as the aortic leaflet tips (landmarks 9, 10 and 11) and mitral leaflet tips (landmarks 15 and 16). The proposed trajectory spectrum learning demonstrates a time consistent and model-independent precision, superior in both cases to reference methods.
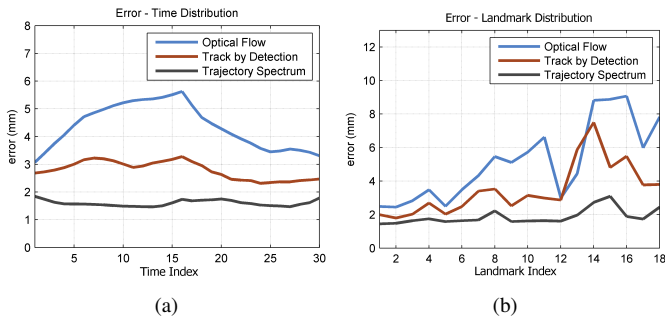

Fig. 14. Error comparison between the optical flow, tracking-by-detection and our trajectory-spectrum approach distributed over (a) time and (b) detected anatomical landmarks. The curve in black shows the performance of our approach, which has the lowest error among all three methods.

C. Quantification Performance and Clinical Evaluation

The quantification precision of the system for the measurements presented in Sec. V is evaluated in comparison to manual expert measurements. Table III shows the accuracy for the Ventriculoarterial Junction, Valsava Sinuses and Sino-tubular Junction aortic root diameters as well as for Annular Circumference, Annular-Posterior Diameter and Anterolateral-Posteromedial Diameter of the mitral valve. The Bland-Altman plots [47] in Fig. 15 demonstrate a strong agreement between manual and model-based measurements for aortic valve areas and mitral annular areas.

Moreover, from a subset of 19 TEE patients, we computed measurements of the aortic-mitral complex and compared those to literature reported values [18]. Distances between the centroids of the aortic and mitral annulae as well as interannular angles were computed. The latter is the angle between the vectors, which point from the highest point of the anterior mitral annulus to the aortic and mitral annular centroids respectively. The mean interannular angle and interannular centroid distance were 137.0 ± 12.2 and 26.5 ± 4.2, respectively compared to 136.2 ± 12.6 and 25.0 ± 3.2 reported in the literature [18].

TABLE III

SYSTEM-PRECISION FOR VARIOUS DIMENSIONS OF THE AORTIC-MITRAL APPARATUS.

	Mean	STD
Ventriculoarterial Junct. $\oslash(cm)$	0.137	0.017
Valsava Sinuses $\oslash(cm)$	0.166	0.043
Sinotubular Junct. $\oslash(cm)$	0.098	0.029
Annular $\vee(cm)$	0.846	0.3
Annular-Posterior $\oslash(cm)$	0.325	0.219
Anterolateral-Posteromedial $\oslash(cm)$	0.509	0.37

$\oslash$ - diameter, $\vee$ - circumferential length.
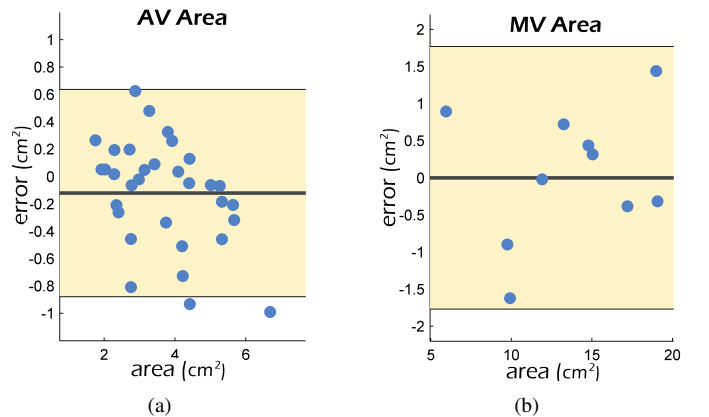

(a)   (b)

Fig. 15. Bland-Altman plots for the (a) aortic valve area and (b) mitral annular area. The aortic valve experiments were performed on CT data from 36 patients, while the mitral valve was evaluated on TEE data from 10 patients, based on the input of a expert cardiologists.

Based on a subgroup of four patients, which underwent both, cardiac CT and TEE, we conducted an inter-modality experiment. To demonstrate the consistency of the model-driven quantification, we obtained the model and measurements from both CT and TEE scans. We included the aortic valve area, inter-commissural distances as well as the Ventriculoarterial Junction, Valsava Sinuses and Sinotubular Junction diameters.
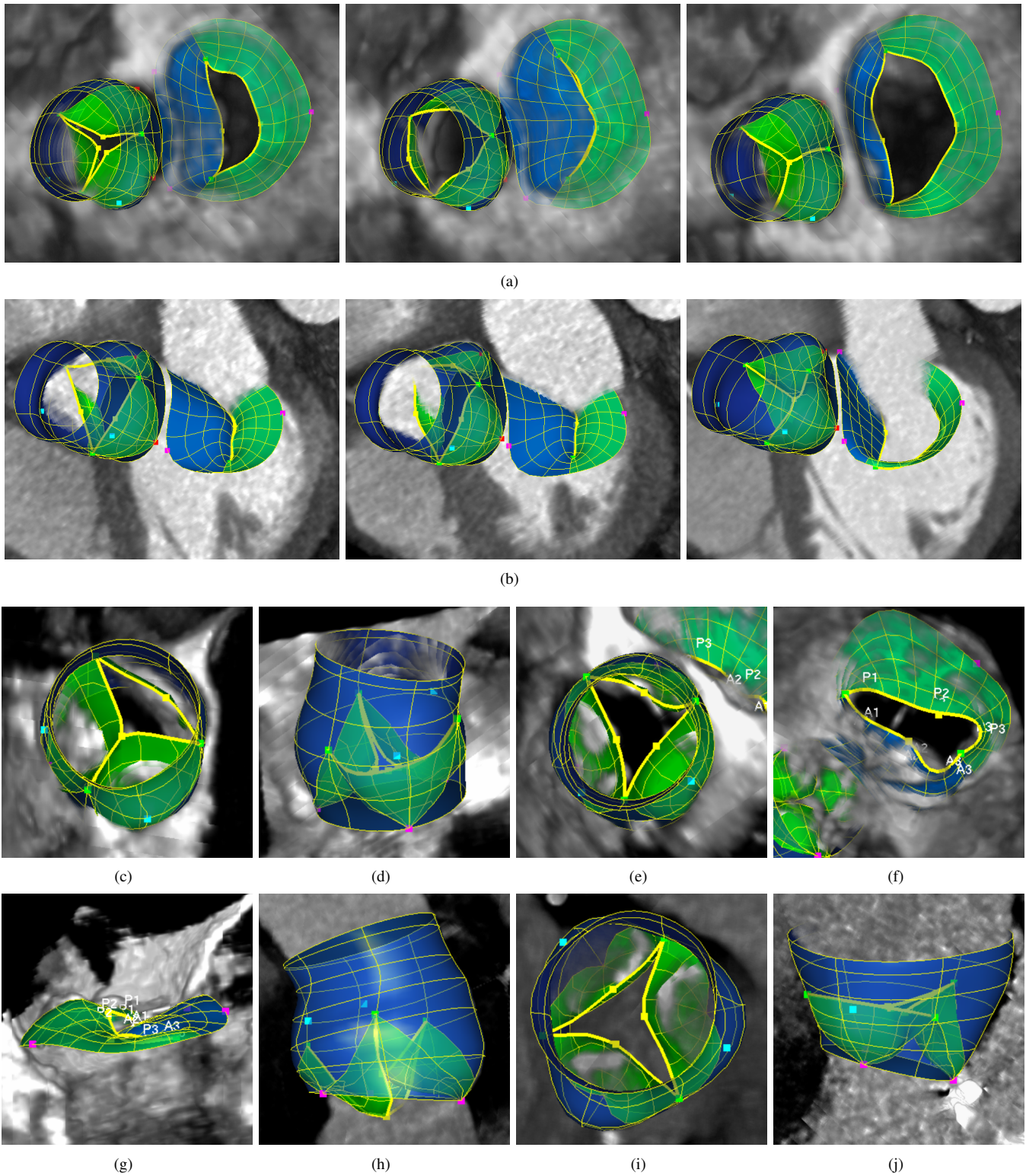
Fig. 13. Examples of estimated patient-specific models from TEE and CT data: healthy valves from three different cardiac phases in (a) TEE from atrial aspect and (b) CT data in four chamber view. Pathologic valves with (c) bicuspid aortic valve, (d) aortic root dilation and regurgitation, (e) moderate aortic stenosis, (f) mitral stenosis, (g) mitral prolapse, (h) bicuspid aortic valve with prolapsing leaflets, (i) aortic stenosis with severe calcification and (j) dilated aortic root.

The experiment demonstrated a strong correlation $r = 0.98$, $p < 0.0001$ and $0.97 - 0.99$ confidence interval.

An inter-user experiment was conducted on a randomly selected subset of ten studies, which have their corresponding patient-specific valve models manually fitted by four experi-enced users. The inter-user variability and system error was computed on four measurements derived from both valves, i.e. the interannular angle and interannular centroid distance discussed earlier in this section, performed in end-diastolic (ED) and end-systolic (ES) phases. The inter-user variability

was determined by computing the standard deviation for each of the four different user measurements and subsequently averaging those to obtain the total variability. To quantify the system error, we compare the automatic measurement result to the mean of the different users. Fig. 16 shows the system-error for the selected sequences with respect to the inter-user variability. Note that except for 3% of the cases, the system-error lies within 90% of the inter-user confidence interval. Thus the variability of measurements obtained by different users on the same data reveals feasible confidence intervals and desired precision of the automated patient-specific modeling algorithm.
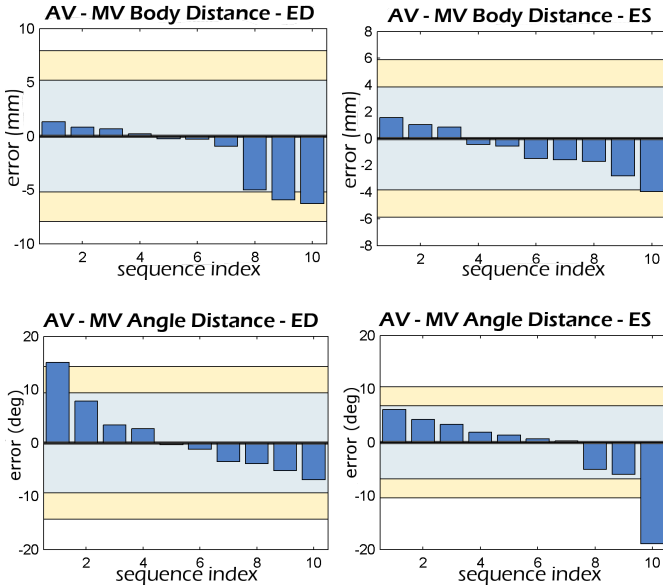

Fig. 16. System error compared to the inter-user variability. The sorted system error (blue bars) and the 80% (light blue area) and 90% (yellow) confidence intervals of the user variability determined from the standard deviation.

Finally, we studied our quantification performance on a patient who underwent a mitral annuloplasty procedure, intended to reduce mitral regurgitation. Pre- and post- TEE exams were performed before and after the successful mitral valve repair. The measurements of the mitral valve area in Fig. 17(a) demonstrates the regurgitant mitral valve to be cured after procedure. Although not explicitly targeted, the intervention had an indirect effect on the aortic valve, also illustrated in Fig. 17(b) by the annular and valvular areas. The observation concurs with clinical findings reported in [3], [4], [18] and shows the converse effect to the one reported by [48], where an intervention on the aortic affected the mitral valve.

VII. Conclusions

This paper presented a novel patient-specific modeling and quantization framework for the aortic and mitral valves, which comprises their full morphology and function. A physiologically-based model allows for an anatomically correct representation of the aortic-mitral valves and their pathological variations. The hierarchical definition of the model facilitates an incremental estimation of patient-specific parameters with increased complexity. The personalized model estimation is automatically performed applying
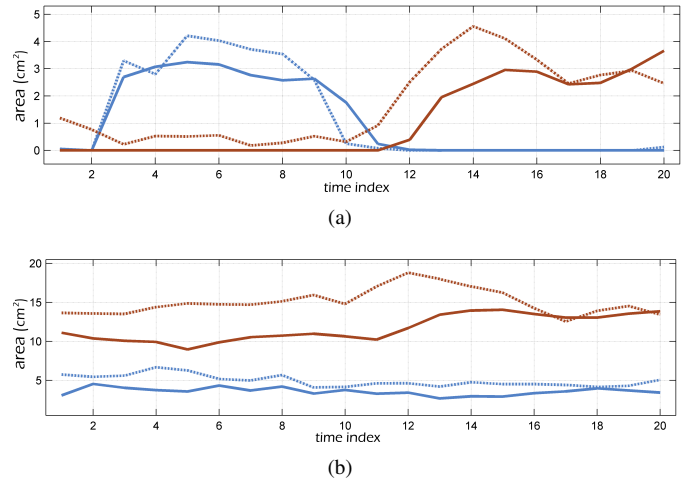

Fig. 17. Measurements obtained before (dotted lines) and after (solid lines) mitral annuloplasty: (a) Aortic (blue) and Mitral (red) valvular area, (b) Aortic (blue) and Mitral (red) annular area.

robust and efficient learning-based algorithms on cardiac 4D CT and TEE data. Especially, the proposed trajectory spectrum learning method enables the simultaneous estimation of spatio-temporal landmark parameters, which is a central problem in computing dynamic models.

From the patient-specific model, we compute for the first time precise **morphological and functional quantification** of the aortic-mitral complex. Extensive experiments performed on a large heterogeneous data set demonstrated a precision of 1.54mm on TEE data and 1.36mm on CT data at a speed of 4.8 seconds per volume. Furthermore, clinical validation showed a strong inter-modality and inter-subject correlation for a comprehensive set of model-based measurements. The method addresses problems of current clinical practice and shows how to overcome these shortcomings. It may not only have impact on the clinical workflow in cardiac health care, such as diagnosis and procedural planning but also design of prosthetic valves and percutaneous interventions for both aortic and mitral valves and may help to understand their interconnection and clinical implications.

ACKNOWLEDGEMENTS

REFERENCES

[1] W. Rosamond, K. Flegal, G. Friday, K. Furie, A. Go, K. Greenlund, N. Haase, M. Ho, V. Howard, B. Kissela, S. Kittner, D. Lloyd-Jones, M. McDermott, J. Meigs, C. Moy, G. Nichol, C.J. O'Donnell, V. Roger, J. Rumsfeld, P. Sorlie, J. Steinberger, T. Thom, S. Wasserthiel-Smoller, and Y. Hong, "Heart disease and stroke statistics–2007 update: a report from the american heart association statistics committee and stroke statistics subcommittee," *Circulation*, vol. 115, no. 5, pp. 69–171, 2007.

[2] R.O. Bonow, B.A. Carabello, K. Chatterjee, A.C.J. de Leon, D.P. Faxon, M.D. Freed, W.H. Gaasch, B.W. Lytle, R.A. Nishimura, P.T. OGara, R.A. ORourke, C.M. Otto, P.M. Shah, and J.S. Shanewise, "Acc/aha 2006 guidelines for the management of patients with valvular heart disease: a report of the american college of cardiology/american heart association task force on practice guidelines (writing committee to develop guidelines for the management of patients with valvular heart disease)," *Circulation*, vol. 114, no. 5, pp. 84–231, 2006.

[3] E. Lansac, K. Lim, Y. Shomura, W. Goetz, H. Lim, N. Rice, H. Saber, and C. Duran, "Dynamic balance of the aortomitral junction," *J Thorac Cardiovasc Surg*, vol. 123, pp. 911–918, 2002.

[4] T. Timek, G. Green, F. Tibayan, F. Lai, F. Rodriguez, D. Liang, G. Daughters, N. Ingels, and D. Miller, "Aorto-mitral annular dynamics," *Ann Thorac Surg*, vol. 76, pp. 1944–1950, 2003.

[5] P. Libby, R.O. Bonow, D.L. Mann, and D.P. Zipes, *Braunwalds's Heart Disease: A Textbook of Cardiovascular Medicine*. Elsevier, 2008.

[6] R.I. Ionasec, Y. Wang, B. Georgescu, I. Voigt, N. Navab, and D. Comaniciu, "Robust motion estimation using trajectory spectrum learning: Application to aortic and mitral valve modeling from 4d tee," in *Proc. Int'l Conf. Computer Vision*, 2009, p. in progress.

[7] R.I. Ionasec, I. Voigt, B. Georgescu, H. Houle, J. Hornegger, N. Navab, and D. Comaniciu, "Modeling and assessment of the aortic-mitral valve coupling from 4d tee and ct," in *Proc. Int'l Conf. Medical Image Computing and Computer Assisted Intervention*, 2009, p. in progress.

[8] R.I. Ionasec, B. Georgescu, E. Gassner, S. Vogt, O. Kutter, M. Scheuering, N. Navab, and D. Comaniciu, "Dynamic model-driven quantification and visual evaluation of the aortic valve from 4d ct," in *Proc. Int'l Conf. Medical Image Computing and Computer Assisted Intervention*, 2008, pp. 686 – 694.

[9] O. Ecabert, J. Peters, and J. Weese, "Modeling shape variability for full heart segmentation in cardiac computed-tomography images," in *Proc. of SPIE Medical Imaging*, vol. 7, no. 2, 2006, pp. 1199–1210.

[10] Y. Zheng, A. Barbu, B. Georgescu, M. Scheuering, and D. Comaniciu, "Four-chamber heart modeling and automatic segmentation for 3d cardiac ct volumes using marginal space learning and steerable features," *IEEE Trans. on Medical Imaging*, vol. 27, no. 11, pp. 1668–1681, 2008.

[11] C. Lorenz and J. von Berg, "A comprehensive shape model of the heart," *Medical Image Analysis*, vol. 10, no. 4, pp. 657–670, 2006.

[12] C.S. Peskin and D.M. McQueen, *Case Studies in Mathematical Modeling: Ecology, Physiology, and Cell Biology*. Englewood Cliffs, NJ, USA: Prentice-Hall, 1996.

[13] J. De Hart, G. Peters, P. Schreurs, and F. Baaijens, "A three-dimensional computational analysis of fluidstructure interaction in the aortic valve," *Journal of Biomechanics*, vol. 36, no. 1, pp. 103–10, 2002.

[14] G. Cacciola, G. Peters, and P. Schreurs, "A three-dimensional mechanical analysis of a stentless fibre-reinforced aortic valve prosthesis," *Journal of Biomechanics*, vol. 33, no. 5, pp. 521–530, 2000.

[15] E. Votta, F. Maisano, S. Bolling, O. Alfieri, F. Montevecchi, and A. Redaelli, "The geoform disease-specific annuloplasty system: A finite element study," *Ann Thorac Surg*, vol. 84, pp. 92–101, 2007, http://dx.doi.org/10.1016/j.athoracsur.2007.03.040.

[16] X. Kuai, J. Zhang, B. Ren, F. Liu, G. Gong, and Y. Zeng, "Stress analysis on stentless quadrileaflet pericardial mitral valve," *Communications in Numerical Methods in Engineering*, 2007, http://dx.doi.org/10.1002/cnm.999.

[17] F. Mahmood, S. Karthik, B. Subramaniam, P. Panzica, J. Mitchell, A. Lerner, K. Jervis, and A. Maslow, "Intraoperative application of geometric three-dimensional mitral valve assessment package: A feasibility study," *Journal of Cardiothoracic and Vascular Anesthesia*, vol. 22, no. 2, pp. 292–298, 2006, http://dx.doi.org/10.1016/S0140-6736(06)69208-8.

[18] F. Veronesi, C. Corsi, L. Sugeng, V. Mor-Avi, E. Caiani, L. Weinert, C. Lamberti, and L.R.M., "A study of functional anatomy of aortic-mitral valve coupling using 3D matrix transesophageal echocardiography," *Circ Cardiovasc Imaging*, vol. 2, no. 1, pp. 24–31, 2009.

[19] T.F. Cootes, C.J. Taylor, D.H. Cooper, and J. Graham, "Active shape models—their training and application," *Computer Vision and Image Understanding*, vol. 61, no. 1, pp. 38–59, 1995.

[20] T.F. Cootes, G.J. Edwards, and C.J. Taylor, "Active appearance models," *IEEE Trans. Pattern Anal. Machine Intell.*, vol. 23, no. 6, pp. 681–685, 2001.

[21] C. Corsi, G. Saracino, A. Sarti, and C. Lamberti, "Left ventricular volume estimation for real-time three-dimensional echocardiography," *IEEE Trans. Medical Imaging*, vol. 21, no. 9, pp. 1202–1208, 2002.

[22] O. Gerard, A.C. Billon, J.-M. Rouet, M. Jacob, M. Fradkin, and C. Allouche, "Efficient model-based quantification of left ventricular function in 3-D echocardiography," *IEEE Trans. Medical Imaging*, vol. 21, no. 9, pp. 1059–1068, 2002.

[23] H.C. v. Assen, M.G. Danilouchkine, A.F. Frangi, S. Ordas, J.J.M. Westenberg, J.H.C. Reiber, and B.P.F. Lelieveldt, "SPASM: A 3DASM for segmentation of sparse and arbitrarily oriented cardiac MRI data," *Medical Image Analysis*, vol. 10, no. 2, pp. 286–303, 2006.

[24] M.d. Bruijne, B.v. Ginneken, M. Viergever, and W. Niessen, "Adapting active shape models for 3d segmentation of tubular structures in medical images," 2003.

[25] A. Fossati, M. Dimitrijevic, V. Lepetit, and P. Fua, "Bridging the gap between detection and tracking for 3D monocular video-based motion capture," in *Proc. IEEE Conf. Computer Vision and Pattern Recognition*, 2007.

[26] L. Taycher, D. Demirdjian, T. Darrell, and G. Shakhnarovich, "Conditional random people: Tracking humans with CRFs and grid filters," in *Proc. IEEE Conf. Computer Vision and Pattern Recognition*, 2006, pp. I: 222–229.

[27] C. Sminchisescu, A. Kanaujia, Z. Li, and D. Metaxas, "Discriminative density propagation for 3D human motion estimation," in *Proc. IEEE Conf. Computer Vision and Pattern Recognition*, 2005, pp. I: 390–397.

[28] L. Wang, X. Geng, C. Leckie, and R. Kotagiri, "Moving shape dynamics: A signal processing perspective," in *Proc. IEEE Conf. Computer Vision and Pattern Recognition*, 2008, pp. 1–8.

[29] I. Akhter, Y. Sheikh, S. Khan, and T. Kanade, "Nonrigid structure from motion in trajectory space," in *Advances in Neural Information Processing Systems*, 2008, pp. 41–48.

[30] L. Zelnik Manor and M. Irani, "Temporal factorization vs. spatial factorization," in *Proc. European Conf. Computer Vision*, 2004, pp. II: 434–445.

[31] A. Naftel and S. Khalid, "Motion trajectory learning in the DFT-coefficient feature space," in *Proc. Int'l Conf. Computer Vision Systems*, 2006, p. 47.

[32] A. Briassouli and N. Ahuja, "Extraction and analysis of multiple periodic motions in video sequences," *IEEE Trans. Pattern Anal. Machine Intell.*, vol. 29, no. 7, pp. 1244–1261, 2007.

[33] Z. Tu, "Probabilistic boosting-tree: Learning discriminative methods for classification, recognition, and clustering," in *Proc. Int'l Conf. Computer Vision*, 2005, pp. 1589–1596.

[34] M. Fischler and R. Bolles, "Random sample consensus: A paradigm for model fitting with applications to image analysis and automated cartography," *Comm. of the ACM*, vol. 24, no. 6, pp. 381–395, June 1981.

[35] P. Viola and M. Jones, "Rapid object detection using a boosted cascade of simple features," in *Proc. IEEE Conf. Computer Vision and Pattern Recognition*, 2001, pp. 511–518.

[36] L. Yang, B. Georgescu, Y. Zheng, P. Meer, and D. Comaniciu, "3d ultrasound tracking of the left ventricle using one-step forward prediction and data fusion of collaborative trackers," in *IEEE Conference on Computer Vision and Pattern Recognition*, 2008.

[37] Z. Tu, X.S. Zhou, A. Barbu, L. Bogoni, and D. Comaniciu, "Probabilistic 3D polyp detection in CT images: The role of sample alignment," in *Proc. IEEE Conf. Computer Vision and Pattern Recognition*, 2006, pp. 1544–1551.

[38] J. Duchon, "Interpolation des fonctions de deux variables suivant le principe de la flexion des plaques minces," *RAIRO Analyse Numerique*, vol. 10, pp. 5–12, 1976.

[39] J.B. Tenenbaum, V. de Silva, and J.C. Langford, "A global geometric framework for nonlinear dimensionality reduction," *Science*, vol. 290, no. 5500, pp. 2319 – 2323, 2000.

[40] M. Akhtar, E.M. Tuzcu, S.R. Kapadia, L.G. Svensson, R.K. Greenberg, E.E. Roselli, S. Halliburton, V. Kurra, P. Schoenhagen, and S. Sola, "Aortic root morphology in patients undergoing percutaneous aortic valve replacement: Evidence of aortic root remodeling," *The Journal of Thoracic and Cardiovascular Surgery*, vol. 137, no. 4, pp. 950 – 956, 2009.

[41] R. Levine, M. Handschumacher, A. Sanfilippo, A.J. ans Hagege, P. Harrigan, J. Marshall, and W.A.E., "Three-dimensional echocardiographic reconstruction of the mitral valve, with implications for mitral valve prolapse," *Circulation*, vol. 80, 1989.

[42] T. Timek, J. Glasson, D. Lai, D. Liang, G. Daughters, N. Ingels, and C. Miller, "Annular height-to-commissural width ratio of annuloplasty rings in vivo," *Circulation*, vol. 112, pp. I–423 – I–428, 2005.

[43] J. Song, S. Fukuda, T. Kihara, M. Shin, M. Garcia, J. Thomas, and T. Shiota, "Value of mitral valve tenting volume determined by real-time three-dimensional echocardiography in patients with functional mitral regurgitation." *American Journal of Cardiology*, vol. 98, no. 8, pp. 1088–1093, 2006.

[44] T.E. David, *Cardiac Surgery in the Adult : Aortic Valve Repair and Aortic ValveSparing Operations*. New York, NY, USA: McGraw-Hill, 2008.

[45] Q. Duan, E. Angelini, S. Homma, and A. Laine, "Validation of optical-flow for quantification of myocardial deformations on simulated RT3D ultrasound," in *ISBI*, 2007.

[46] T. Zhao and R. Nevatia, "3D tracking of human locomotion: a tracking as recognition approach," in *ICPR*, 2002, pp. I: 546–551.

[47] J. Bland and D. Altman, "Statistical methods for assessing agreement between two methods of clinical measurement," *Lancet*, 1986.

[48] F. Vanden-Eynden, D. Bouchard, I. El-Hamamsy, A. Butnaru, P. Demers, M. Carrier, L. Perrault, J. Tardif, and M. Pellerin, "Effect of aortic valve replacement for aortic stenosis on severity of mitral regurgitation." *Ann Thorac Surg*, vol. 83, pp. 1279–84, 2007.